Combustion Science and Technology

ISSN: 0010-2202 (Print) 1563-521X (Online) Journal homepage: https://www.tandfonline.com/loi/gcst20

Spray Combustion Characteristics of Palm Biodiesel

Cheng Tung Chong & Simone Hochgreb

To cite this article: Cheng Tung Chong & Simone Hochgreb (2012) Spray Combustion Characteristics of Palm Biodiesel, Combustion Science and Technology, 184:7-8, 1093-1107, DOI: 10.1080/00102202.2012.663999

To link to this article: https://doi.org/10.1080/00102202.2012.663999

Combust. Sci. Technol., 184: 1093–1107, 2012

ISSN: 0010-2202 print/1563-521X online
DOI: 10.1080/00102202.2012.663999

Taylor & Francis
Taylor & Francis Group

SPRAY COMBUSTION CHARACTERISTICS OF PALM BIODIESEL

Cheng Tung Chong[1,2] and Simone Hochgreb[2]

[1]*Faculty of Mechanical Engineering, Universiti Teknologi Malaysia, Skudai, Johor, Malaysia*

[2]*Hopkinson Lab, Department of Engineering, University of Cambridge, Cambridge, UK*

The potential of palm methyl esters (PME) as an alternative fuel for gas turbines is investigated using a swirl burner. The main air flow is preheated to 623 K, and a swirling spray flame is established at atmospheric pressure. The spray combustion characteristics of PME are compared to diesel and Jet-A1 fuel under the same burner power output of 6 kW. Investigation of the fuel atomizing characteristics using phase Doppler anemometry (PDA) shows that most droplets are distributed within the flame reaction zone region. PME droplets exhibit higher Sautermean diameter (SMD) values than baseline fuels, and thus higher droplet penetration length and longer evaporation timescales. The PME swirl flame presents a different visible flame reaction zone while combusting with low luminosity and produces no soot. NO_x emissions per unit mass of fuel and per unit energy are reduced by using PME relative to those of conventional fuels.

Keywords: Airblast; Gas turbine; Jet-A1; Palm biodiesel; Spray flame; Swirl burner

INTRODUCTION

Concerns about the rising fuel price and global climate change have led to the search for alternative fuels and energy sources. Biodiesel is recognized as a viable substitute for diesel fuel. The growing importance of biodiesel is shown through the increasing annual productions and blending mandates that have been implemented in various countries (REN21, 2010). Biodiesel can be produced from vegetable and animal oils through a transesterification process, in which the triglycerides from vegetable oils react with methanol to form methyl esters and glycerol (Van Gerpen et al., 2004). Depending on the feedstock, the biodiesel produced typically consists of a mixture of several methyl esters. The physical properties of biodiesel are comparable to those of diesel, albeit with lower heating values. For this reason, biodiesel can be used neat or as a blend with diesel in compression ignition engines. It was reported

Received 30 March 2011; revised 3 December 2011; accepted 1 February 2012.

Published as part of the Seventh Mediterranean Combustion Symposium Special Issue with Guest Editors Federico Beretta, Nevin Selçuk, Mohy S. Mansour, and Andrea D'Anna.

Address correspondence to Cheng Tung Chong, Faculty of Mechanical Engineering, Universiti Teknologi Malaysia, 81310 Skudai, Johor, Malaysia. E-mail: ctchong@mail.fkm.utm.my

that biodiesel is able to reproduce the desired efficiency as diesel fuel but with higher fuel specific consumption (Xue et al., 2011). Lower emissions of soot, CO, and CO_2 but higher NO_x were achieved by using biodiesel (Nabi et al., 2006; Xue et al., 2011).

Although biodiesel is mainly used in diesel blends in compression-ignition engines, application in gas turbine engines or furnaces for power generation is further envisaged. The feasibility of using biodiesels in gas turbines has been shown in field tests. Molière et al. (2007) demonstrated that NO_x emission of rapeseed biodiesel is lower compared to diesel fuel in a 40 MW gas turbine. The emissions of CO and NO for soy, palm biodiesel, and 20% biodiesel blend with diesel are reported to be similar in a semiclosed cycle gas turbine field test (Ellis et al., 2008). Implementation of emission mitigation measures requires detailed understanding of the combustion characteristics of different fuels.

Krishna (2007) examined the emissions of soy biodiesel and blends of soy biodiesel with diesel fuel in a 30 kW micro gas turbine engine (Capstone C30) test. The results showed reduction of CO and NO emissions for biodiesel and blends and no loss of thermal efficiency. However, Bolszo and McDonell (2009) reported an increase of NO_x emissions when soy biodiesel was used instead of diesel, but that improved NO_x emissions could be achieved by increasing the mass ratio of the atomizing air to liquid fuel. The conflicting results show that a more in-depth investigation of biodiesel combustion is needed.

There have been a few combustion tests on biodiesel conducted using swirl burners. Sequera et al. (2008) investigated the emissions of diesel, soy methyl ester, soy ethyl ester, and bio-oil pyrolized from hardwood. Their results demonstrated that biodiesel blended fuels emitted lower NO_x and CO at conditions where the fuel flow rates are kept constant. Similar trends of emission reduction using biodiesel were observed in experiments conducted by Panchasara et al. (2009). It was reported that the reduction of NO emission of biodiesel is associated with the lower flame temperature that is achieved with the increase of atomizing air. Hashimoto et al. (2008) investigated the emissions of palm biodiesel relative to diesel in a gas turbine–type burner. The result indicates that NO emission for palm biodiesel is consistently lower compared to diesel fuel when plotted as a function of excess air ratio, droplet Sauter mean diameter (SMD), atomizing air pressure, and viscosity. These results indicate that biodiesel produces lower NO_x emissions than diesel fuel under gas turbine conditions, contrary to the higher NO_x emissions measured in compression-ignition engine experiments (Canakci, 2007; Nabi et al., 2006).

In this article, the combustion characteristics of palm biodiesel are investigated under the swirling spray flame conditions using phase Doppler anemometry (PDA) and flame imaging techniques. The data obtained can be used as validation targets for biodiesel swirl flame modeling as well as practical combustor or injector design. The emission performance of the PME relative to baseline fuels is also investigated.

EXPERIMENTAL

Burner and Flow Delivery

The swirl burner in this experiment consists of a circular quartz tube forming the combustor wall and a swirler at the burner outlet. The axial swirler consists of eight

straight vanes fixed at the angle of 45°, which generate strong swirl intensity. The geometric swirl number, S_N, is calculated as 0.78 based on the following equation:

$$S_N = \frac{2}{3}\left[\frac{1-(D_h/D_s)^3}{1-(D_h/D_s)^2}\right]\tan\theta$$

where D_h and D_s represent the swirler hub diameter and the swirler diameter, respectively, and θ is the angle of the swirl blade from the centerline (Beer and Chigier, 1972). A plain-jet airblast atomizer (Delavan, SN type-30610-1) is placed concentrically with the swirler. The diameters of the air and fuel orifice are 1.73 mm and 0.5 mm, respectively. The swirl vanes and airblast nozzle are flush mounted to the burner face as shown in Figure 1a. The swirler is held by a central tube, designed for delivering atomizing air and liquid to the atomizer. The liquid spray generated from the atomizer is enveloped by the swirling air coaxially. The atomizing air and fuel flows are independently controlled. The fuel flow rate is accurately supplied to the atomizer via a Bronkhorst Coriolis mass flow controllers (M13 mini CORI-FLOW), with an accuracy of $\pm 0.4\%$. The main air flow and atomizing air are separately regulated by two Bronkhorst thermal mass flow controllers (MFC), which deliver the full scale accuracy of $\pm 1\%$ respectively. The schematic of the single swirl flame burner configuration and flow delivery system is presented in Figure 1b.

The main air flow is heated by two in-line air heaters (750 W/heater) arranged in series. The burner plenum and body are additionally heated by three Omega rope heaters (500 W/rope) and insulated with high temperature heat-resisting materials to reduce heat loss. A 1.5 mm diameter thermocouple is placed 10 mm under the swirler to measure the temperature of the main air. The heating facility allows the main air to be preheated to a temperature of 350°C. The signal from the thermocouple provides the feedback control to the temperature controller of the air heaters. The uncertainty of the temperature associated with the preheated air is within ±5 K. The whole burner is constructed using stainless steel.

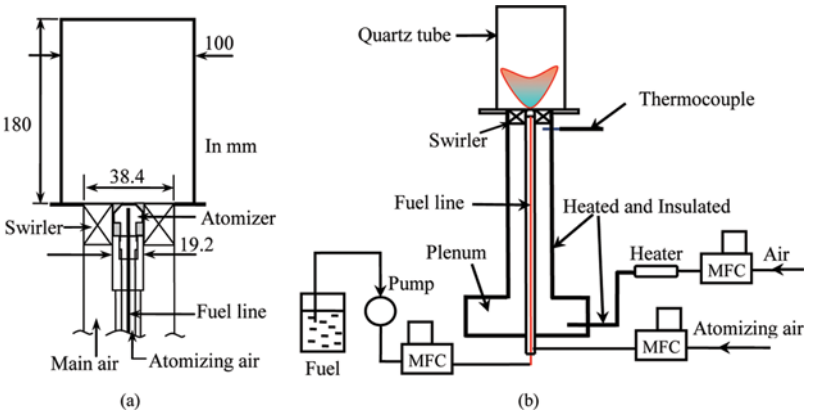

Figure 1 (a) Geometry of the swirl burner and (b) schematic of the flow delivery system. (Figure is provided in color online.)

Fuel

Biodiesel is typically composed of a mixture of methyl esters with no aromatic rings or sulfur. Due to the presence of oxygen in the molecules, biodiesels have lower heating values compared to conventional petroleum fuels. The winter grade palm biodiesel/methyl esters (PME) used in this experiment are supplied by Carotino Sdn. Bhd. Malaysia. The PME conforms to the European Union's EN14214 standard with the approximated composition of 43.1% methyl oleate, 39.5% methyl palmitate, 10.4% methyl linoleate, and 5% methyl stearate (Gopinath et al., 2009). Jet-A1 fuel is a light distillate fuel that consists of complex hydrocarbon mixtures of 50–65% paraffins, 10–20% aromatics, and 20–30% naphthenes (Dagaut et al., 2006). The standard Jet-A1 fuel used here is sourced from Conoco Limited, UK. Another conventional fuel tested here is diesel fuel. The present commercial grade low-sulfur diesel fuel is obtained from a Shell petrol station in the UK. The typical composition of diesel fuel is 25–50% of paraffins, 20–40% of cycloparaffins, and 15–40% of aromatics (Farrell et al., 2007). Comparison of the properties of biodiesel with conventional fuels is shown in Table 1. PME has higher density and viscosity compared to diesel. The low volatility of PME is reflected by the relatively high flash point of 174°C. The ignition delay time of PME is shorter than diesel, as indicated by the higher cetane number. The composition of C/H/O for PME is 77.3/12.2/10.5% by weight based on the laboratory microanalysis result.

Operating Conditions

The main bulk swirling air flow is preheated to a temperature of 350°C while the liquid fuel and atomizing air are delivered to the atomizer at room temperature. The interaction of the swirling air flow with the liquid spray forms a globally lean mixture. To compare the combustion characteristics of the fuels, the flames are established at the same power output condition. The air and fuel mass flow rates are metered accordingly based on the fuel's energy content to obtain the burner power output at 6 kW while maintaining a global equivalence ratio of $\varphi = 0.47$. In the case of PME, the fuel flow rate is increased by 17% due to lower heating values to maintain

Table 1 Properties of diesel, Jet-A1, and PME

Properties	Jet-A1	Diesel	PME
Approx. formula	$C_{11}H_{21}$	$C_{16}H_{34}$	$C_{19}H_{36}O_2$
H/C ratio*	1.98	1.9	1.89
C/O ratio*	–	–	9.83
Spec. grav. 15°C	0.81	0.85	0.88
Viscosity 40°C (cSt)	–	2.6	4.5
Pour point (°C)	–	–20	–18
Flash point (°C)	38	60–72	174
Boiling range (°C)	166–266	190–360	>215
LHV (kJ/kg)	43150	43090	36770
Cetane number	–	52	62.6

*Laboratory analysis.

Table 2 Operating conditions

Fuel	Main air (g/s)	Fuel (g/s)	Atomizing air (g/s)	Global φ	Power (kW)
Diesel	4.15	0.14	0.28	0.47	6.0
Jet-A1	4.09	0.14	0.28	0.47	6.0
PME	4.04	0.16	0.32	0.47	6.0

the same conditions as diesel and Jet-A1, as indicated in Table 2. The atomizing air-to-fuel mass flow rate ratio (ALR) is set constant at 2.0 for all test cases.

Phase Doppler Anemometry (PDA)

The simultaneous measurement of droplet velocity and size is performed using PDA. The droplet size is determined based on the measured phase shift difference between two Doppler bursts, whereas the droplet velocity is obtained from the Doppler burst frequency (Durst and Zare, 1975). The 1D PDA (Dantec 112 mm Fiber PDA) consists of a continuous-wave Argon-ion laser (Coherent, Innova 70C) that produces a laser beam at 514.5 nm. The beam from the laser is split into two almost identical beams via a beam splitter. A 500 mm focal lens is used to form a measurement volume at the intersection point of the beams. The receiving optics that house the detectors are positioned at 56° off-axis to the transmitter to capture the light scattered from the droplets. Table 3 shows the beam transmitter and the optical settings for the PDA system. Both the transmitting and receiving optics are mounted onto a 3-D traverse system with stepper motors that have the spatial accuracy of $\pm$ 0.1 mm. The PDA measurement was performed within the flames established at the burner outlet. Measurements were taken at axial positions of 10, 15, and 20 mm downstream of the burner outlet, as indicated in Figure 2. Locations close to the spray outlet were not measured, as the dense spray region may cause the PDA measurements to be unreliable. A minimum of 2000 data points were taken for each spatial point along the radial profiles. The statistical uncertainty is estimated to be 2% and 5% for the droplets velocity and diameters, respectively, which could be due to optical misalignment or

Table 3 PDA optical setting

Transmitting optics	
Wavelength	514.5 nm
Power	0.8 W
Beam spacing	45 mm
Beam width	2.2 mm
Focal length	500 mm
Number of fringes	26
Width of measurement vol.	0.149 mm
Length of measurement vol.	3.312 mm
Receiving optics	
Focal length	310 mm
Scattering angle	56°

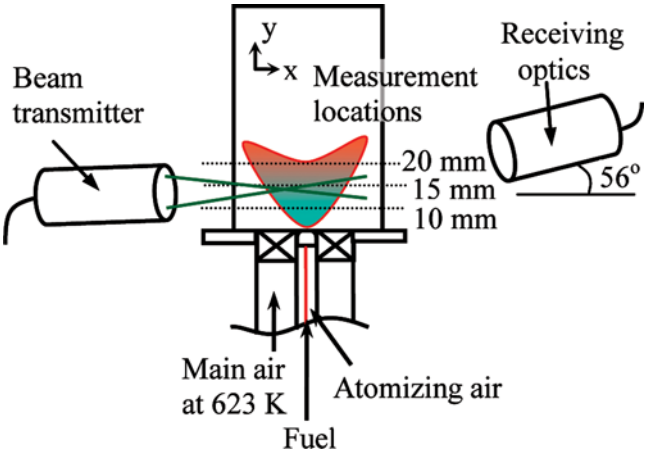

Figure 2 PDA setup and measurement locations. (Figure is provided in color online.)

setting errors in photomultiplier (Zhang and Ziada, 2000). Validation rates determined by the PDA software for the droplets' velocity and sizes were at least 90%. For volume flux measurements, the present uncertainty is estimated to be 30% based on the comparison of the integrated volume flux and the volume flow rate under nonreacting spray. The uncertainty is attributable to the nonuniform intensity distribution (Gaussian beam effect) in the measurement volume, suppressed scattered light due to slit aperture (slit effect), and the miscalculation of cross-sectional area (Zhang and Ziada, 2000). Sampling statistics for the volume flux should be extensive to prevent undersampling of droplets in larger bins.

RESULTS AND DISCUSSION

Droplet Velocity and SMD Profiles

Measurements of the spray characteristics of reacting flows established from diesel, Jet-A1, and PME fuels were performed under fixed power output conditions. The droplet velocity and SMD profiles on one side of the centerline are shown in Figure 3 for 10, 15, and 20 mm from the burner outlet. The x-abscissa indicates the radial profile from the centerline ($x = 0$ mm) of the burner. At 10 mm from burner exit, the droplet velocity peaks at the radial position of 3 mm as shown in Figure 3a. The droplet axial velocity profile then decreases as the radial distance increases from the centerline. At a further downstream location of 15 mm, the velocity peak appears at a wider radial distance as a result of the interaction of the spray with the main swirling flow as shown in Figure 3b. The strong radial flow from the swirling flow induces a radial pressure gradient, in which the central recirculation zone is formed while the spray spreads radially. The strong reverse flow at the centerline region interacts with the droplets, which lowers the droplet velocity further downstream.

Diesel exhibits a similar droplet velocity and SMD profiles as PME at locations 10 and 15 mm downstream of the spray outlet. A low SMD value is observed at the centerline region but gradually increases with increasing radial positions. Between the

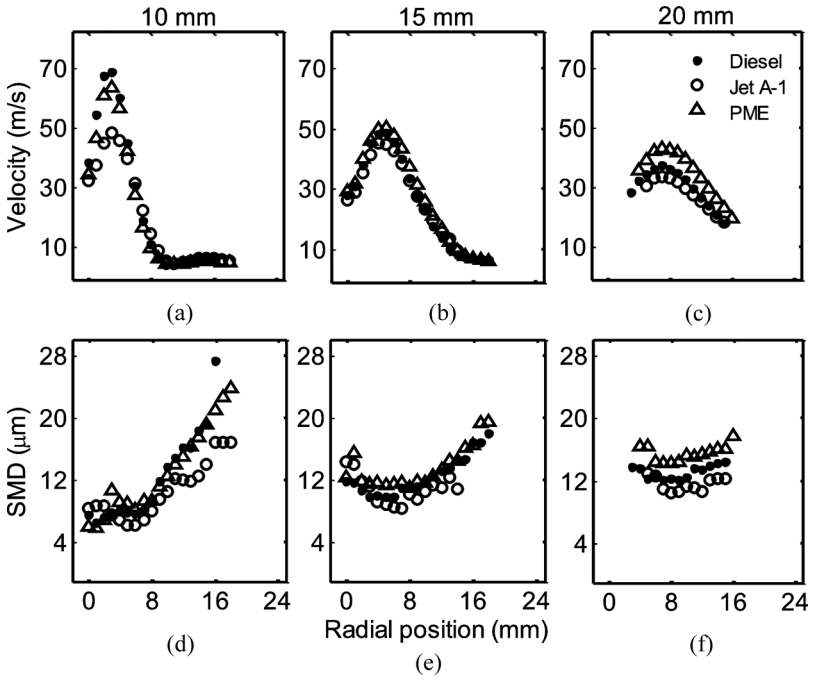

Figure 3 Droplet axial velocity (a,b,c) and SMD profiles (d,e,f) for diesel, Jet-A1, and PME flames established under constant power conditions for three different heights from the burner face.

radial position at 8 mm and the centerline, the droplets are distributed within the intense heat release region. The heat propagated from the reaction zone assists in vaporizing the small droplets within this region. At the radial position of 5 mm, which coincides with the location of maximum volume flux, a slight increase of SMD values for diesel and PME is observed.

At the downstream location of 20 mm, the difference between droplet velocity and size becomes more obvious, as presented in Figures 3c and 3f. PME droplets show higher SMD and velocity values than diesel droplets at the same spatial locations. The larger SMD value for PME droplets is due to the influence of higher viscosity and surface tension values compared to diesel fuel. The small and scarce droplets at the centerline and periphery region have completely vaporized, whereas the high droplet density region sustains some larger droplets. The remaining large PME droplets contain higher momentum and thus enable longer penetration length with extended evaporation time.

Jet-A1 flame shows a slightly lower velocity and SMD values compared to diesel and PME fuels at all axial locations. This is because Jet-A1 fuel is more volatile and has a lower boiling point value compared to the heavier hydrocarbons. Hence, droplet vaporization occurs in a relatively shorter time scale due to the higher dispersion rate and smaller droplet size. The smaller droplets contain lower velocity due to the loss of momentum as the downstream axial distance increases.

The droplet size and axial velocity distribution superimposed on the mean CH^* chemiluminescence intensity are shown in Figures 4a and 4b for Jet-A1 and PME

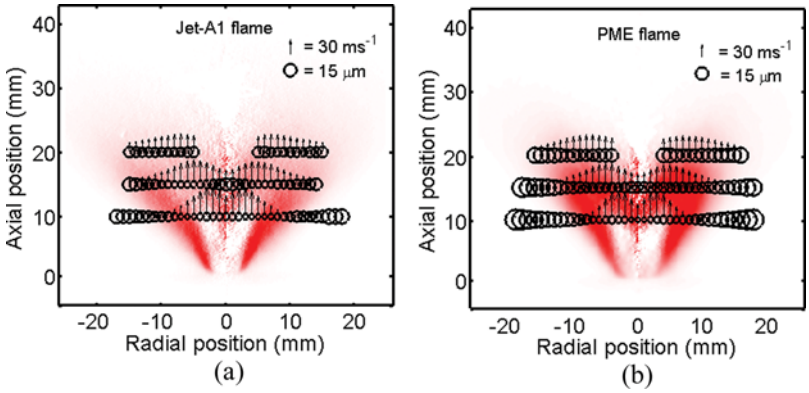

Figure 4 Droplet velocity and size distribution within the (a) Jet-A1 and (b) PME swirl flames superimposed on the corresponding CH^* chemiluminescence signals. (Figure is provided in color online.)

flames, respectively. Despite the different shape of the heat release zone shown by the CH^* chemiluminescence signal, the overall droplet distribution is rather similar. Small droplets are distributed within the reaction zone, while bigger droplets are located outside the flame zone. The intense heat within the flame facilitates evaporation of droplets. At the downstream location of 20 mm, droplets at the center region are completely vaporized, and no further CH^* chemiluminescence is detectable. The larger droplets outside the flame zone appear at much lower velocity than the smaller droplets at the center region of the flame. The high droplet velocity at the centerline region is attributed to the high momentum attained from the atomizing air. The PME flame shows an overall larger droplet distribution compared to the Jet-A1 flame.

Droplet Concentration and Volume Flux

The droplet number density and volume flux profiles of the spray flames at the axial locations 10, 15, and 20 mm downstream of burner outlet are shown in Figure 5. The distribution at all downstream axial locations indicates that droplet concentration peaks at a distance away from the centerline ($x = 0$ mm). The PME flame presents higher peak droplet number density than diesel and Jet-A1 by factors of two and four, respectively, at the spatial radial position of 7 mm as shown in Figure 5a. The high droplet density and volume flux is partly due to the higher mass flow rates of PME by $\sim 17\%$ compared the baseline fuels under constant power output condition of 6 kW. The remaining larger PME droplets that are not completely vaporized also contribute to the droplet density count. Jet-A1 fuel shows lower droplet number density and volume flux present in the flame due to the high volatility of the fuel, which facilitates vaporization.

Despite the slight difference of droplet SMD profiles between diesel and PME (Figure 3), the droplet concentration and volume flux are observed to be lower for diesel at all spatial locations. The droplet density peaks shift from radial position 7 mm to 9 mm between downstream axial locations of 15 and 20 mm due to the radial spreading of the spray. In regions where the droplet number density is high, rapid mixing with air creates a leaner mixture for reactions. This is shown in Figure 4 where

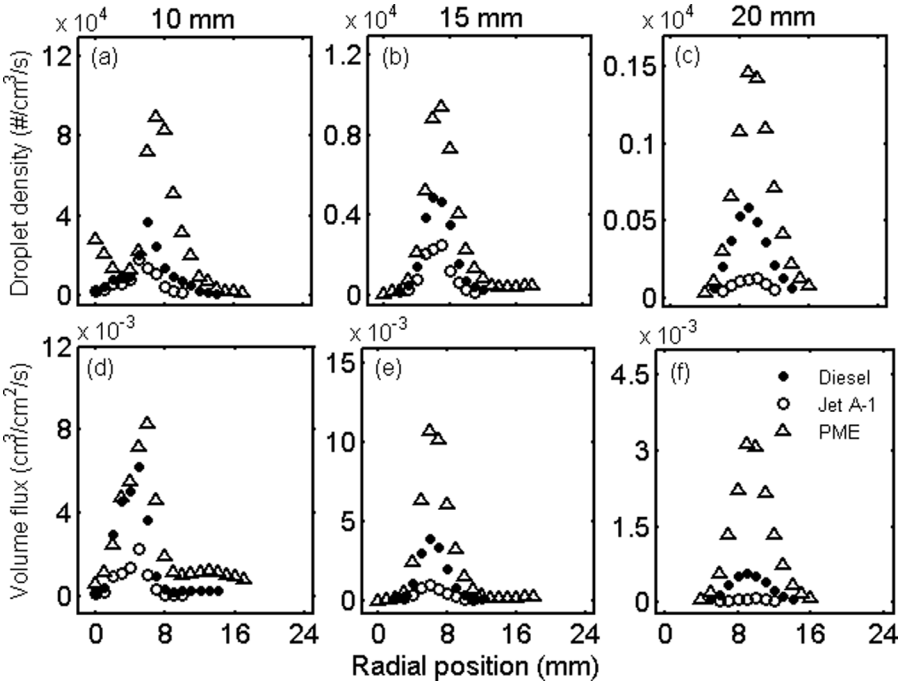

Figure 5 Droplet number density (a,b,c) and volume flux(d,e,f) profiles at axial locations 10, 15, and 20 mm from burner outlet under the power output of 6 kW. Note the different *y*-scales on each figure.

the intense heat reaction zone corresponds to the locations where the droplet density peaks. Away from the flame zone ($x > 10$ mm), the droplets exhibit larger SMD values, but the droplet number density and volume flux distribution in these regions is very low as shown in Figure 5. The CH^* chemiluminescence intensity peaks at locations where the droplet density is high but with relatively small droplets. This suggests that the variation of the spray droplet distribution and concentration has significant influence on the flame shape and reaction zone.

Flame Imaging

The global flame structure of liquid swirl flames was imaged via line-of-sight CH^* chemiluminescence (430 ± 10 nm) and broadband spectrum (>550 nm) using an intensified CCD camera. The obtained line-of-sight images were averaged (300 images) and deconvoluted via Abel transformation to obtain the planar flame structures. The excited CH^* chemiluminescence from the flames can be used as an indicator of heat release rate (Hardalupas and Orain, 2004). Figure 6 shows the planar flame structures for diesel, Jet-A1, and PME swirl flames, respectively. The Jet-A1 flame exhibits a heat release zone of similar shape to diesel, but with a slightly wider flame angle. The PME flame presents a more locally intense central flame front. The high intensity of the CH^* emission for PME could be due to the late vaporization of droplets and higher localized diffusion flames.

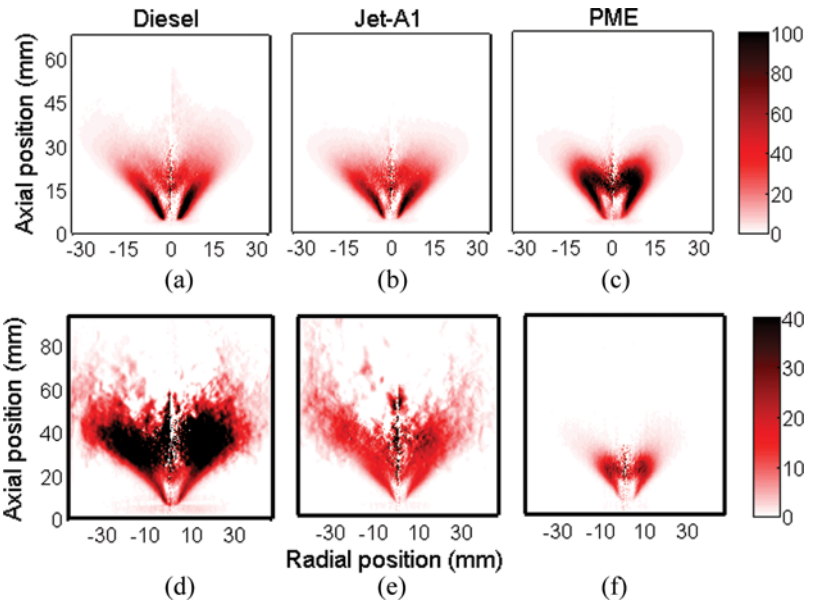

Figure 6 Abel transformed (a,b,c) CH^* chemiluminescence and (d,e,f) longpass filtered (>550 nm) imaging. (Figure is provided in color online.)

The length of all the flame reaction zones based on CH^* chemiluminescence is approximately 30 mm downstream of the burner outlet. This demonstrates that the highest local flame temperature occurs in a relatively similar spatial region within the combustor. Complete vaporization and consumption of droplets occurs within this region despite the difference in fuel source. The corresponding half-plane radial CH^* intensity profiles at 4, 8, 13, and 17 mm from the burner outlet are presented in Figure 7, where $x = 0$ mm indicates the centerline of the burner. The Jet-A1 flame shows similar CH^* intensity profiles at 13 and 17 mm as diesel flame, but with lower intensity peaks at axial profiles of 4 and 8 mm. The PME flame shows similar intensity profiles at 4 and 8 mm as Jet-A1, but higher intensity at 13 and 17 mm compared to both Jet-A1 and diesel flames.

As most of the spectral intensity of the flame is distributed in the form of thermal radiation continuous spectra of 550 nm and beyond, a CCD camera coupled with a broadband longpass filter is used to image the region where soot is present. The longpass filtered images of Jet-A1, diesel, and PME are presented in Figures 6d–6f. Jet-A1 and diesel flames present a sooty region downstream of the reaction flame zone, but the latter shows much higher intensity than the former due to the high sooting tendency. From observation, both fuels establish a bluish flame near the burner outlet (where the intense heat release occurs) and a luminous yellow flame downstream. The bluish premixed flame near the flame root is the typical characteristics of twin-fluid atomizer where the atomizing air enhances mixing with droplets (Lefebvre, 1980). The intense luminosity is attributed to the soot radiation as a result of high content of aromatic rings in diesel (~20–40%) and Jet-A1 fuel (~10–20%).

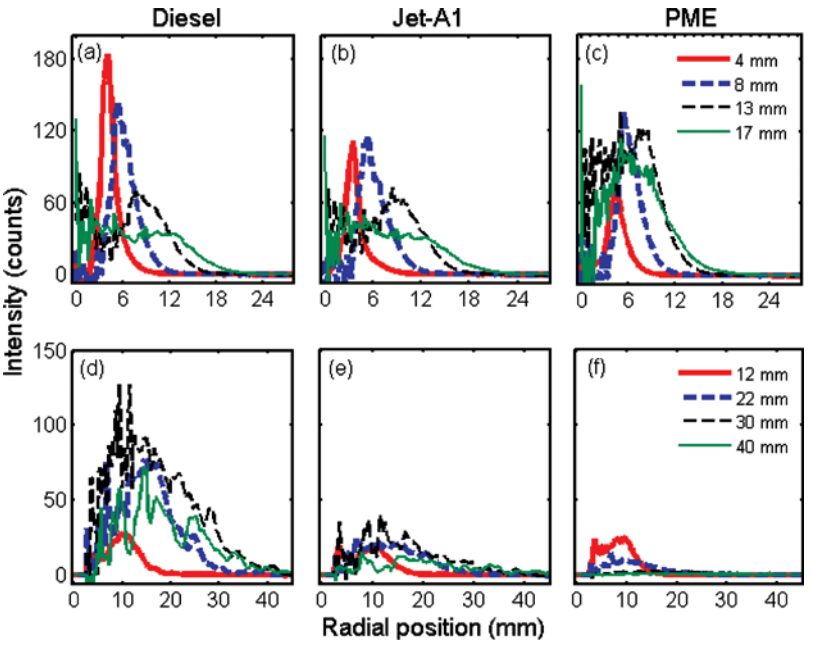

Figure 7 Intensity profiles of (a,b,c) CH^* chemiluminescence and (d,e,f) longpass filtered (>550 nm) signals for diesel, Jet-A1, and PME swirl flames under the power output of 6 kW. (Figure is provided in color online.)

In contrast, the PME flame exhibits no sign of soot within the combustor. The flame shows only the bluish region equivalent to a premixed flame. The image shown in Figure 6f indicates that the intensity is mainly emitted from the heat release zone. The low luminosity of the palm biodiesel flame has also been observed by Hashimoto et al. (2008) in a swirling flame investigation established using a pressure-swirl nozzle. The presence of oxygen in palm biodiesel enhances the local premixed combustion of hydrocarbon with oxygen, whereas the absence of aromatic rings inhibits the formation of soot and the sooty yellowish flame brush downstream. It has also been reported that the soot generated from biodiesel is rapidly oxidized due to the initial incorporation of oxygen groups in the molecule (Song et al., 2006).

The intensity profiles of longpass signals (>550 nm) at 12, 22, 30, and 40 mm downstream of burner outlet are shown in Figures 7d, 7e, and 7f for diesel, Jet-A1, and PME flames, respectively. The diesel flame shows higher flame intensity by a factor of three compared to the Jet-A1 flame. The highest intensity is found to occur at the profile of 30 mm downstream of the burner exit for both flames, whereas PME shows no sign of soot at this particular region. The only intense region in the PME flame (12 mm downstream) coincides with the reaction zone, and the profile is similar to those shown in Jet-A1 flame at the same spatial location.

Flame Spectroscopy

Flame emission spectroscopy was performed by spectrally resolving the flame spectrum into UV and near-infrared range (~200–900 nm). The global flame spectrum

signal was focused onto the slit of a spectrometer (USB2000 + ; Ocean Optics) via a focusing lens. Figure 8 shows the global flame spectra obtained from diesel, Jet-A1, and PME swirl flames. All flames show discrete peaks due to excited radicals. The diesel flame shows a prominent rising baseline between 550 and 850 nm due to the intense luminosity radiated by the soot. The peak around visible wavelength of 600 nm indicates the color spectrum of yellow-orange as observed in the flame. The Jet-A1 flame shows a reduced intensity for the soot band by half compared to the diesel flame. The obtained flame spectroscopy concurs with the spatially resolved long bandpass (>550 nm) filtered images as shown in Figure 6 where the soot formation for the Jet-A1 flame is lower than the diesel flame. The PME flame is characterized as soot-free based on the near-zero intensity between the wavelength band of 580 and 900 nm.

Emission Measurements

The post-combustion emissions of CO, NO, and NO_2 were measured using a Tocsin 320 gas analyzer at the combustor outlet. A sampling probe of 4 mm in diameter was placed 10 mm inward from the burner exit to sample across the burner outlet. The area-velocity-weighted emissions values were obtained from five equally spaced positions with 2 min of sampling time for each spatial location. The sampling line was preheated to 180°C and insulated to prevent condensation of post-combustion products.

Due to the variation of power density between the fuels, scaling to same power output and fuel/air mass ratio yields the global equivalence ratio of 0.47, 0.47, and 0.40 for diesel, Jet-A1, and PME flames, respectively. The atomizing air to liquid mass

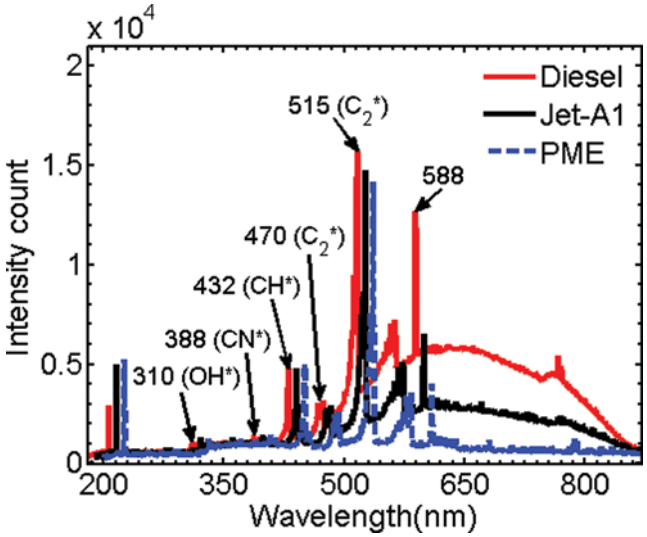

Figure 8 Flame emission spectroscopy measurements compared under the same power output conditions of 6 kW. The spectra of Jet-A1 and PME are displaced along the wavelength axis by + 10 and +20 nm, respectively, for clarity. (Figure is provided in color online.)

ratio was maintained at 2.0 for all test cases, while the total air/fuel mass ratio was 32. The emission results of NO, NO_2, and CO obtained as a function of power output and area-velocity weighted are shown in Figure 9. The emission indexes are expressed in emissions per unit kg of fuel (Figures 9a–9c) and kWh (Figures 9d–9f).

The PME flame shows a slight reduction of NO and NO_2 emissions compared to diesel and Jet-A1 flames when expressed in per mass of fuel burned. Due to the lower heating value of PME, the emission index is slightly higher on a per-unit energy basis. Even so, the emissions of NO and NO_2 is lower when compared to diesel and Jet-A1.

The reduction of NO_x emissions per unit mass and per unit heating value using PME fuel under spray flame conditions has also been reported by Hashimoto et al. (2008). The peak stoichiometric flame temperatures for PME (2564 K) are similar to those of diesel (2559 K) and Jet-A1 (2587 K) (Chong and Hochgreb, 2011). Since PME droplets are slightly larger, as indicated in Figure 3, one would expect, if anything, for NO_x emissions to be higher for PME than hydrocarbon fuels. However, the oxygen in PME may suppress CH production, thus reducing prompt NO_x sufficiently to create an overall reduction. PME contains no aromatic ring, and the flame is characterized by near-zero soot as shown in the long pass filtered (>550 nm) signals in Figure 6f and the sootless spectra in Figure 8. Diesel and Jet-A1 flames exhibit relatively similar NO, NO_2, and CO emissions.

NO emissions decrease as the power output increases, as shown in Figures 9a and 9d. The reduction of NO at higher power output is most likely a result of the reduced residence times as the flow rates increase. A slight increasing trend in CO

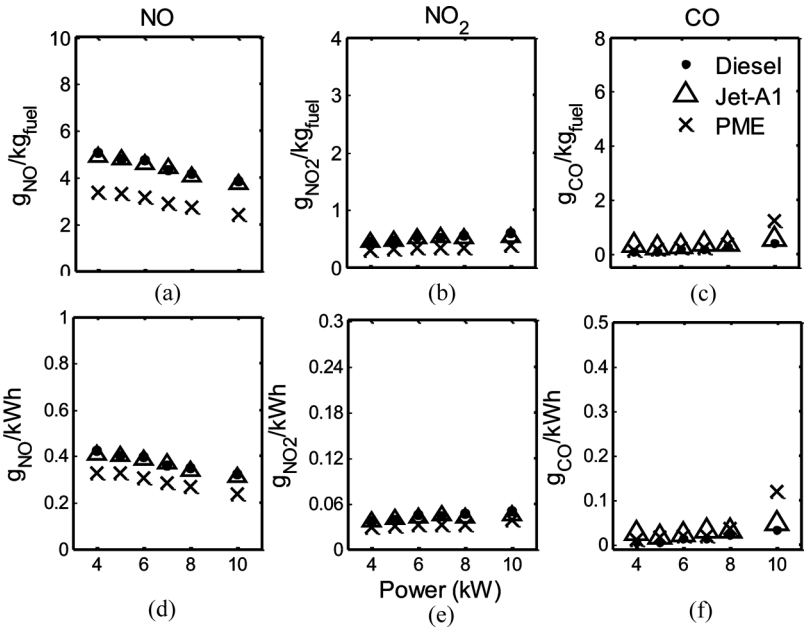

Figure 9 Emission indices for NO, NO_2, and CO as a function of burner power output expressed in (a–c) mass per unit mass of fuel and (d–f) mass per unit energy. AFR = 32, ALR = 2.0, $\varphi = 0.47$ for diesel and Jet A-1, and $\varphi = 0.40$ for PME.

emission is observed, possibly for similar reasons, as CO has less time to oxidize. NO_2 is present at an order of magnitude lower than NO, with the emission values that are almost constant with the increase of power output.

CONCLUSIONS

The spray combustion characteristics of PME have been compared to diesel and Jet-A1 flames under the same power output condition. The droplets within the reacting flames are characterized using a PDA system. The interaction of the recirculation flow and the droplets causes the lower droplet velocity at the centerline region. The flame reaction zone coincides with spatial positions where the droplets density and volume flux are high. PME droplets show slightly higher SMD values than baseline fuels with higher droplet concentration and volume flux. The swirl flame generated from PME shows a bluish, low luminosity flame without a yellow sooty region. From CH^* chemiluminescence imaging, the PME flame shows a more intense localized heat release region than flames established from conventional fuels. Longpass filtered ($>$550 nm) imaging shows no sign of soot for the PME swirl flame, as supported by the spectrally resolved flame spectra. Emissions measurements indicate that PME produces lower NO_x per unit mass of fuel and per unit energy under overall lean mixture, continuous, swirling spray flame conditions.

ACKNOWLEDGMENTS

The financial support from the Ministry of Science, Technology and Innovation (MOSTI) Malaysia (project number: 03-01-06-KHAS01) is gratefully acknowledged. The author would like to thank Prof. Gyung-Min Choi from Pusan National University for fruitful discussions.

REFERENCES

Beer, J.M., and Chigier, N.A. 1972. *Combustion Aerodynamics*, Applied Science Publ., London.

Bolszo, C.D., and McDonell, V.G. 2009. Emissions optimization of a biodiesel fired gas turbine. *Proc. Combust. Inst.*, **32**, 2949–2956.

Canakci, M. 2007. Combustion characteristics of a turbocharged DI compression ignition engine fueled with petroleum diesel fuels and biodiesel. *Bioresour. Technol.*, **98**, 1167–1175.

Chong, C.T., and Hochgreb, S. 2011. Measurements of the laminar flame speeds of liquid fuels: Jet-A1, diesel, palm methyl esters, and blends using particle imaging velocimetry (PIV). *Proc. Combust. Inst.*, **33**, 979–986.

Dagaut, P., El Bakali, A., and Ristori, A. 2006. The combustion of kerosene: Experimental results and kinetic modelling using 1- to 3-component surrogate model fuels. *Fuel*, **85**, 944–956.

Durst, F., and Zare, M. 1975. Laser Doppler measurements in two-phase flows: The accuracy of flow measurements by laser Doppler methods. In *Proceedings of the LDA-Symposium*, August 25–28, Copenhagen, Denmark, A76-45326 23-35, pp. 403–429.

Ellis, W., Lear, W., Singh, B., Srinivasan, A., Crittenden, J., and Sherif, S. 2008. Flameless combustion of biofuels in a semi-closed cycle gas turbine. Presented at the 46th AIAA Aerospace Sciences Meeting and Exhibit, January 7–10, Reno, Nevada.

Farrell, J.T., Cernansky, N.P., Dryer, F.L., Friend, D.G., Hergart, C.A., Law, C.K., McDavid, R.M., Mueller, C.J., Patel, A.K., and Pitsch, H. 2007. *Development of an experimental database and kinetic models for surrogate diesel fuels*. SAE Paper 2007–01-0201, 2007 SAE World Congress.

Gopinath, A., Puhan, S., and Nagarajan, G. 2009. Relating the cetane number of biodiesel fuels to their fatty acid composition: a critical study. *Proceedings of the Institute of Mechanical Engineering, Part D: Journal of Automobile Engineering*, **223**, 565–583.

Hardalupas, Y., and Orain, M. 2004. Local measurements of the time-dependent heat release rate and equivalence ratio using chemiluminescent emission from a flame. *Combust. Flame*, **139**, 188–207.

Hashimoto, N., Ozawa, Y., Mori, N., Yuri, I., and Hisamatsu, T. 2008. Fundamental combustion characteristics of palm methyl ester (PME) as alternative fuel for gas turbines. *Fuel*, **87**, 3373–3378.

Krishna, C.R. 2007. *Performance of the capstone C30 microturbine on biodiesel blends*, Brookhaven National Laboratory, Upton, NY.

Lefebvre, A.H. 1980. Airblast atomization. *Prog. Energy Combust. Sci.*, **6**, 233–261.

Molière, M., Panarotto, E., Aboujaib, M., Bisseaud, J.M., Campbell, A., Citeno, J., Maire, P., and Ducrest, L. 2007. *Gas turbine in alternative fuel applications: Biodiesel field test*. Presented at the ASME Turbo Expo 2007: Power for Land, Sea, and Air, May 14–17, Montreal, Canada.

Nabi, M.N., Akhter, M.S., and Zaglul Shahadat, M.M. 2006. Improvement of engine emissions with conventional diesel fuel and diesel-biodiesel blends. *Bioresour. Technol.*, **97**, 372–378.

Panchasara, H.V., Simmons, B.M., Agrawal, A.K., Spear, S.K., and Daly, D.T. 2009. Combustion performance of biodiesel and diesel-vegetable oil blends in a simulated gas turbine burner. *J. Eng. Gas Turbines Power*, **131**, 031503.1–031503.11.

REN21. 2010. Renewables 2010 global status report. REN21 Secretariat, Paris.

Sequera, D., Agrawal, A.K., Spear, S.K., and Daly, D.T. 2008. Combustion performance of liquid biofuels in a swirl-stabilized burner. *J. Eng. Gas Turbines Power*, **130**, 032810.1–032810.10.

Song, J., Alam, M., Boehman, A.L., and Kim, U. (2006). Examination of the oxidation behaviour of biodiesel soot. *Combust. Flame*, **146**, 589–604.

Van Gerpen, J., Shanks, B., Pruszko, R., Clements, D., and Knothe, G. 2004. Biodiesel production technology. NREL/SR-510–36244. National Renewable Energy Laboratory, Golden, CO.

Xue, J., Grift, T.E., and Hansen, A.C. 2011. Effect of biodiesel on engine performances and emissions. *Renew. Sust. Energy Rev.*, **15**, 1098–1116.

Zhang, Z., and Ziada, S. 2000. PDA measurements of droplet size and mass flux in the three-dimensional atomization region of water jet in air-cross flow. *Exp. Fluids*, **28**, 29–35.